



Cobalt ion implantation assisted modifications in luminescence, surface states, structural and morphological properties of MgTiO₃ thin films

Deepak Negi¹ · Radhe Shyam¹ · Komal Shekhawat¹ · Subingya Pandey² · Pamu Dobbidi² · Pargam Vashishtha³ · Govind Gupta³ · Devarani Devi⁴ · Fouran Singh⁴ · Srinivasa Rao Nelamarri¹

Received: 23 September 2022 / Accepted: 14 April 2023 / Published online: 2 May 2023
© The Author(s), under exclusive licence to Springer-Verlag GmbH, DE part of Springer Nature 2023

Abstract

In the present work, the effects of ion implantation on structural, surface, optical, and photoluminescence behavior of MgTiO₃ thin films have been investigated. Cobalt ions were implanted into crystalline films by varying the fluence from 3×10^{14} to 1×10^{16} ions/cm². An intensity reduction and shift of the peak position upon implantation are attributed to amorphization and generation of strain, respectively. The root-mean-square roughness is reduced from 8.2 (pristine) to 6.4 nm upon implantation at 3×10^{14} ions/cm² fluence and increases to 7.9 nm with a further upsurge in fluence. A non-monotonous variation in transmittance with implantation fluence is observed. The bandgap of pristine sample is ~4.22 eV, and the implanted samples exhibit a bandgap in the range of 4.03–3.88 eV. The surface chemical states of pristine and implanted films were analyzed using X-ray photoelectron spectroscopy. An enhancement in defects upon implantation of Co ions results in the variation of luminescence properties. A broad photoluminescence (PL) emission band extending from near UV to visible region is observed for the pristine film. The PL emission intensity is quenched upon implantation. Average decay lifetime of pristine film is observed to be 17.9 ns, which is slightly increased to 19.1 ns at 3×10^{14} ions/cm² implantation fluence. Afterward, with a subsequent rise in implantation fluence from 1×10^{15} to 1×10^{16} ions/cm², the average decay lifetime varied within the range of 17.2–18.9 ns. Factors responsible for different luminescent centers, structure, and morphology evolution as a consequence of Co ion implantation are reported.

Keywords MTO thin films · Ion implantation · Atomic force microscopy · X-ray photoelectron spectroscopy · UV–Vis–NIR spectroscopy · Photoluminescence

1 Introduction

MgTiO₃ (MTO) is a well-known ceramic material, which received a considerable attention for different industrial applications due to its promising properties, such as a wide bandgap [1], thermal stability [2], a near zero temperature coefficient of resonant frequency, and a high quality factor (Q) [3]. Over past few decades, a lot of research work on bulk, powdered, and thin films of MTO has been carried out to achieve desired characteristics for various applications, such as dielectric resonators at microwave frequencies, filters [4], wireless communication [5], global positioning system, integrated circuits [6], FRAMs [7], photocatalytic material [8], sensors, etc. Apart from this, MTO is interestingly focused to explore its photoluminescence properties to be utilized in several optical applications due to its low phonon frequency (which may reduce non-radiative

✉ Srinivasa Rao Nelamarri
srnelamarri.phy@mnit.ac.in

¹ Department of Physics, Malaviya National Institute of Technology Jaipur, J. L. N. Marg, Jaipur 302017, Rajasthan, India
² Department of Physics, Indian Institute of Technology Guwahati, Guwahati 781039, Assam, India
³ CSIR-National Physical Laboratory, K.S. Krishnan Marg, New Delhi 110012, India
⁴ Inter-University Accelerator Centre, Aruna Asaf Ali Marg, New Delhi 110067, India

transitions) as well as thermal and chemical stability [9]. It finds applications in display devices, solid state lighting, and white LEDs with different dopants, such as Eu^{3+} , Al^{3+} , and Dy^{3+} , Li^+ [9, 10]. The dopant elements are generally chosen according to their compatibility with the host matrix. The low solution energy of Co doping in MTO makes it one of the easily doped and well-suited dopants in the MTO matrix [11]. Apart from it, J. H. Sohn et al. reported that Co doped MTO possesses a slightly higher Q-factor as compared to pure MTO [12]. Also, T. S. Kumar et al. showed the applicability of Co doped MTO in complementary metal-oxide semiconductors and anti-reflection coatings [13]. In addition, the decreased leakage current density is observed in Co doped MTO [14]. On the basis of earlier reports, it becomes imperative to study the MTO thin films with incorporation of optically active Co ions and their effects on optical properties from the application point of view. Y. N. Shieh et al. showed the effective rearrangement of charge distribution as a result of Co ion implantation into the TiO_2 matrix, which improves the PL intensity [15]. In addition, 300 keV Co ions were implanted into Zn doped TiO_2 films, and the modification in bandgap with Co ions incorporation was demonstrated [16]. Moreover, the shift in bandgap and various emission centers in TiO_2 are observed, which are a consequence of transition involving the d levels of Co ions [17]. On the other hand, R. Kumar et al. studied luminescence properties and bandgap variation in ZnO with Co ions implantation, and showed the applicability of Co implanted ZnO thin films in spintronic oriented devices [18]. Therefore, apart from ease and compatibility of Co ions into MTO, it also showed significant improvement in the properties of other matrices.

In the present work, we have incorporated Co ions into the MTO matrix using ion implantation. Ion implantation is an alternative doping approach in which the dopants with some fixed fluence or dose can be added into the host matrix at a desired depth. Moreover, a precise control over ion fluence, and the possibility of overcoming the solubility limit are unique advantages [19]. In general, the nuclear energy loss (S_n) plays a major role for modifications of a material, in case of low energy ion implantation process. A large number of defects (interstitials and vacancies) are generated inside the matrix as a result of cascade collisions with incident energetic ions [20], which can effectively tune the bandgap, luminescent centers, and surface chemistry of the film. The photoluminescence (PL) efficiency and emission centers are found to be quite sensitive to the dopants and their concentration. Therefore, it becomes interestingly important to study the implantation induced evolution in structure and morphology, which in turn effects the luminescent behavior and optical properties of MTO thin films. Moreover, an absence of reports on the ion implantation of pure MTO thin films motivated to carry out the study. In the present work,

Co ions with 100 keV energy were implanted into MTO matrix at different fluences, i.e., 3×10^{14} , 1×10^{15} , 3×10^{15} , and 1×10^{16} ions/cm². The effects of incorporation of Co ions on luminescent properties, optical bandgap, as well as structure and morphology modification of MTO films, were studied in detail.

2 Materials and methods

2.1 Synthesis of samples

MTO thin films were synthesized using RF magnetron sputtering unit (Advanced Process Technology, Pune). Before the deposition process, the evacuation of sputtering chamber was carried out using rotary and turbo molecular pumps to a base pressure of $\sim 1.52 \times 10^{-5}$ mbar. The deposition was carried out at RF power of 85 W. The process pressure of nearly 7.4×10^{-3} mbar was maintained throughout the deposition. Afterward, conventional furnace annealing at 750 °C was carried out to crystallize the as-deposited MTO thin films. The thickness of the film is around 530 nm.

2.2 Implantation

Furthermore, 100 keV Co ions were implanted into pristine films (annealed at 750 °C) at various fluences, such as 3×10^{14} , 1×10^{15} , 3×10^{15} , and 1×10^{16} ions/cm². The implantation of thin film samples was carried out using low energy ion beam facility at Inter-University Accelerator Centre (IUAC), New Delhi. The projected range, and nuclear and electronic energy losses were estimated using SRIM 2008 simulation software, which are found to be ~ 50 nm, and 1.5 and 0.2 keV/nm, respectively.

2.3 Characterizations

After implantation, characterization of pristine and implanted samples was done using X-ray diffraction (XRD; TTRAX III, Rigaku, Japan) to examine the variation in crystalline nature of MTO thin films with implantation fluence. XRD measurements were carried out using Cu K_α monochromatic X-ray source with wavelength of 1.54 Å. The step size and scan speed during the measurements were 0.02° and $3^\circ/\text{min}$, respectively. The impact of implantation fluence on surface morphology was analyzed using atomic force microscope (AFM; Multimode Scanning Probe Microscope, Bruker). In addition, optical bandgap and other optical parameters were deduced using UV–Vis–NIR spectroscopy. The surface chemistry of MTO thin films was studied with X-ray photoelectron spectroscopy (XPS; Omicron Nanotechnology, ESCA+, Germany) with 1486.6 eV monochromatic Al K_α source. During XPS measurements,

the base pressure was around 5.2×10^{-10} mbar. The pass energy of 50 eV was utilized for the survey scan, while the short scan was carried out with energy of 20 eV. Energy resolution of XPS is about 0.6 eV. To overcome the charging effect, a charge neutralizer of 2 keV is applied and binding energy of C1s core was taken as reference. Moreover, the photoluminescence PL spectroscopy was carried out with 310 nm wavelength excitation source using 450 W Xenon flash lamp. In addition, the time-resolved PL of films was done using 266 nm pulsed laser excitation source (FLS980 Edinburgh system) to estimate the decay lifetime of pristine and implanted samples.

3 Results and discussion

3.1 XRD analysis

Figure 1a indicates the XRD pattern of pristine, and Co ion implanted MTO thin films at different fluences within the range of 3×10^{14} to 1×10^{16} ions/cm². Pristine MTO thin film shows the XRD peaks indexed as (003), (101), (012), (104), (110), (113), (024), (107), (116), (018), (214), and (300) situated at 18.9°, 21.1°, 23.9°, 32.8°, 35.4°, 40.6°, 49.1°, 50.3°, 53.5°, 56.9°, 62°, and 63.7°, respectively. The observed well defined peaks indicate the rhombohedral crystal structure of MTO thin films with $R\bar{3}$ space group and are matched with the standard database (reference JCPDS #000,060,494). The crystalline quality of films is found to deteriorate upon ion implantation, followed by an increase in fluence, as shown in Fig. 1a. Implantation is observed to induce defects, such as vacancies

and dislocations, etc., into the films [21, 22]. The disorders and/or defects generated in the samples are proportional to the fluence of implanted ions [23, 24]. Therefore, with an increase in fluence, the defect density increases, which causes strain in the sample leading to the disturbance of long-range order in the matrix. Such a disturbance eventually deteriorates the crystallinity of the films which is evident from the reduction in intensity of peaks in the XRD pattern [22, 25]. A minor shift in the position of peaks, as displayed in Fig. 1b, indicates the generation of tensile strain in the films upon implantation [21, 22]. During implantation, some of the implanted Co²⁺ ions will possibly substitute Mg²⁺ (having comparable ionic radii) in the octahedral coordination geometry. The ionic radius of Co²⁺ is 0.75 Å, which is slightly larger as compared to Mg²⁺ with an ionic radius of 0.72 Å. As a result, the lattice parameter is observed to expand slightly, which probably leads to the generation of tensile strain in the films. Such an observation of generation of tensile strain upon ion implantation is also reported in the literature [19, 21, 26]. A minor reversible change in the strain is observed at higher fluence which possibly occurred as a result of slight contraction of lattice due to the irradiation led compressive in-plane stress. A similar observation is also reported for CdTe and NiO thin films [27, 28].

The crystallite size was evaluated using Scherrer's equation [29] given as

$$D = \frac{K\lambda}{\beta \cos\theta} \quad (1)$$

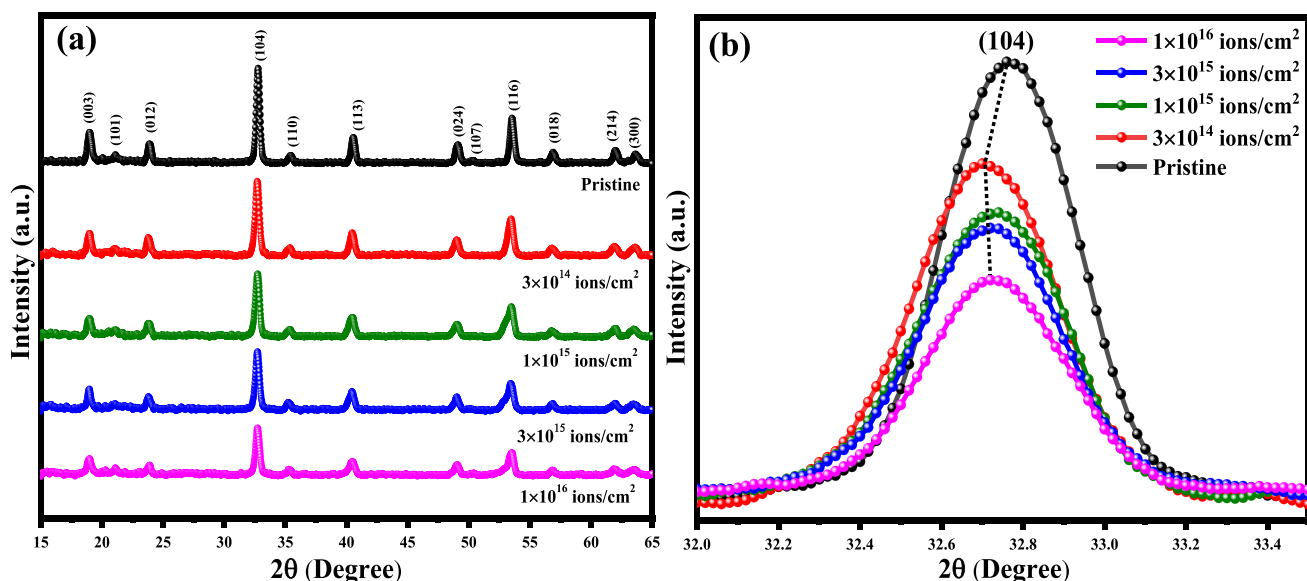


Fig. 1 a XRD pattern of pristine, and implanted films with Co ions at various fluences within the range 3×10^{14} to 1×10^{16} ions/cm², b peak shifting in highly oriented (104) peak

where K denotes the shape factor whose value is 0.9, which is considered for the samples consisting of both cubic and noncubic crystallites [30], λ indicates the incident X-ray wavelength, full-width at half maximum intensity in radians is denoted as β , and θ is the Bragg angle. Pristine sample exhibits the crystallite size of $\sim 21.8 \pm 0.2$ nm, which is decreased to 19.2 ± 0.2 nm upon implantation of Co ions at a fluence of 3×10^{14} ions/cm². Implantation induced cascade collisions result in multiple displacements in the matrix, which may cause a reduction in the size of crystallites. Further, a monotonic increase in the crystallite size from 19.2 ± 0.2 nm to 19.8 ± 0.2 nm after an increase of implantation fluence from 3×10^{14} to 1×10^{16} ions/cm² is observed. The increase in crystallite size upon increasing the fluence is possibly due to energy deposition to the lattice as a result of ion–solid interaction, where incident ions impart energy to the sample causing an increase in temperature, which leads to a slight increase in crystallite size. A similar observation of variation of crystallite size with implantation fluence was also reported for CdTe thin films [28].

3.2 AFM results

The morphology evolution of MTO thin films, as depicted in Fig. 2a–e, prior to and after Co ion implantation, has been deduced from AFM. Various competing processes like surface erosion by ion bombardment and diffusion of adatoms are responsible for the reorganization of films' surface [31].

The surface becomes rough or smooth depending upon the energy and fluence of arriving ions during implantation [32].

The root-mean-square roughness (R_q) of pristine film is 8.2 nm, which is found to reduce to 6.4 nm after implantation at 3×10^{14} ions/cm² fluence. While it is slightly increased to 7 nm upon increasing the fluence to 1×10^{15} ions/cm². There is no significant variation of roughness for the films implanted at 1×10^{15} and 3×10^{15} ions/cm². A subsequent rise in fluence to 1×10^{16} ions/cm², the R_q is significantly enhanced to 7.9 nm. It is observed that with implantation of Co ions into the films, R_q first decreases and then increases (shown in Fig. 2f) with a rise in the fluence. This particular behavior in R_q can be understood on the basis of adatoms' mobility over the surface which is influenced by the impact of ion beam. The adatoms get activated, and their mobility is increased, resulting in diffusion of adatoms to fill the inner voids at the surface, which lead to the reduction in surface roughness at a fluence of 3×10^{14} ions/cm². Furthermore, implantation at higher fluence results in rise of temperature due to which the adatoms jump over the upper layers increasing the surface roughness of samples [32]. The increase in surface roughness can also be attributed to the sputtering of atoms, more likely from the valleys as an impact of ion implantation [33, 34].

The grain size distribution and average diameter of grains measured using AFM micrographs, are indicated in Fig. 3. A reduction in grain size from 76 ± 2 nm (pristine film) to 72 ± 2 nm is noticed upon implantation and increasing the

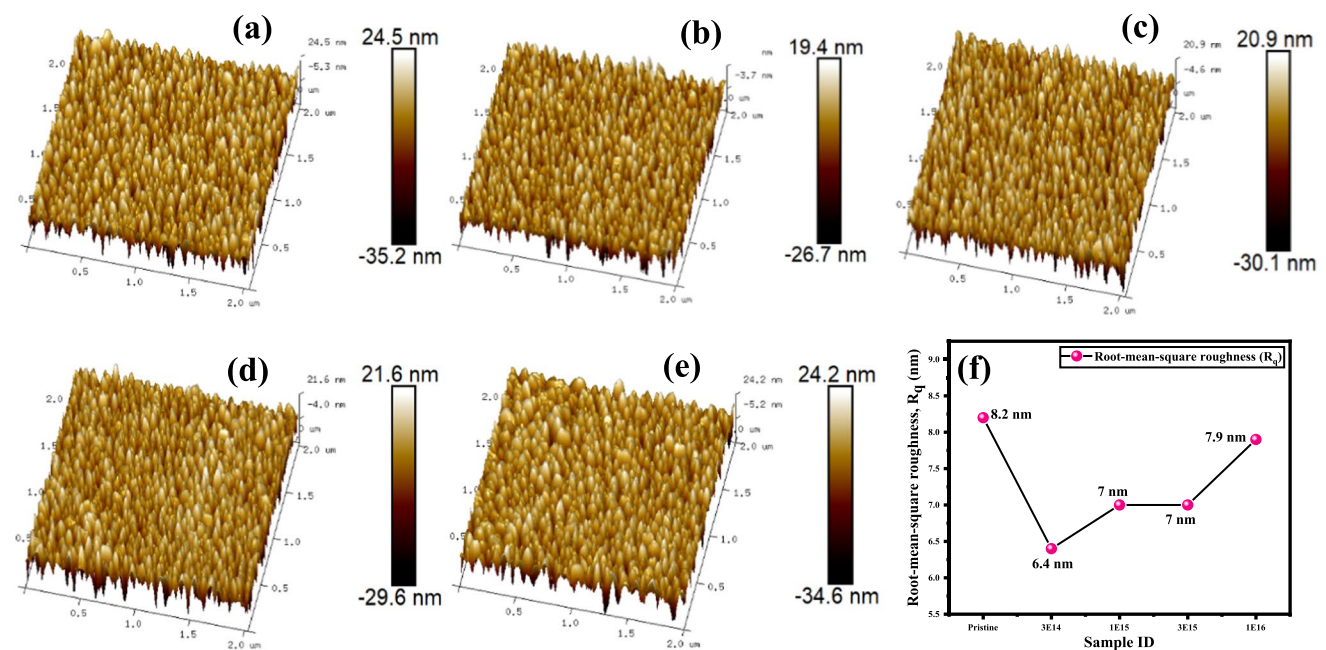


Fig. 2 AFM micrographs of **a** pristine, and Co ion implanted MTOence of implanted ions [here, 3E14, 1E15, 3E15, and 1E16 represent the samples at different fluences of **b–e** 3×10^{14} , 1×10^{15} , 3×10^{15} , and fluence of 3×10^{14} , 1×10^{15} , 3×10^{15} and 1×10^{16} ions/cm²]. **f** Variation in root-mean-square roughness with flu-

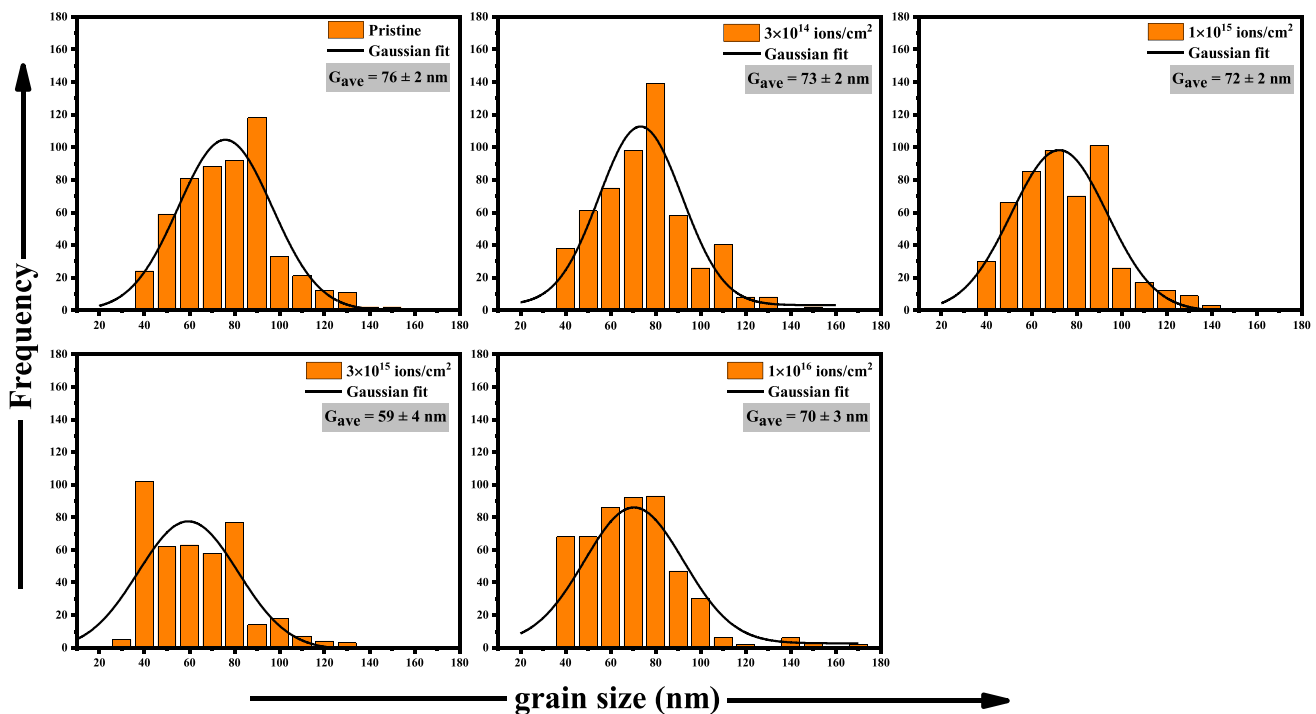


Fig. 3 Grain size distribution of pristine and implanted MTO thin film samples

fluence to 1×10^{15} ions/cm². A further rise in fluence to 3×10^{15} ions/cm², significantly reduces the size to 59 ± 4 nm. The reduction in grain size up to the fluence 3×10^{15} ions/cm² is attributed to the fragmentation of grains because of generation of internal strain upon implantation [35]. Afterward, an enhancement in grain size to 70 ± 3 nm is observed which is due to the agglomerations of fragmented grains as a result of increased surface energy [35].

3.3 UV-Vis-NIR spectroscopy

Transmittance spectra of the films (pristine and implanted) are obtained in the range of 250–800 nm, as shown in Fig. 4. Pristine film exhibits transmittance of ~59–97% in the visible region. The transmittance goes on to increase slightly up to ~63–97% upon embedding Co ions in the film at 3×10^{14} ions/cm² implantation fluence. Subsequently, transmittance percentage is reduced to ~62–94% and ~59–84% for implanted films at 1×10^{15} and 1×10^{16} ions/cm² fluences, respectively. The roughness of the films is one of the crucial factors responsible for variation in transmittance. More the roughness, higher will be the transmittance scattering loss [36, 37]. The decreased roughness of film implanted at a fluence of 3×10^{14} ions/cm² results in higher transmittance. In the same way, upon implantation at a fluence of 1×10^{15} ions/cm², film shows a slight rise in transmittance as compared to pristine film, while lower transmittance as compared to 3×10^{14} ions/cm²

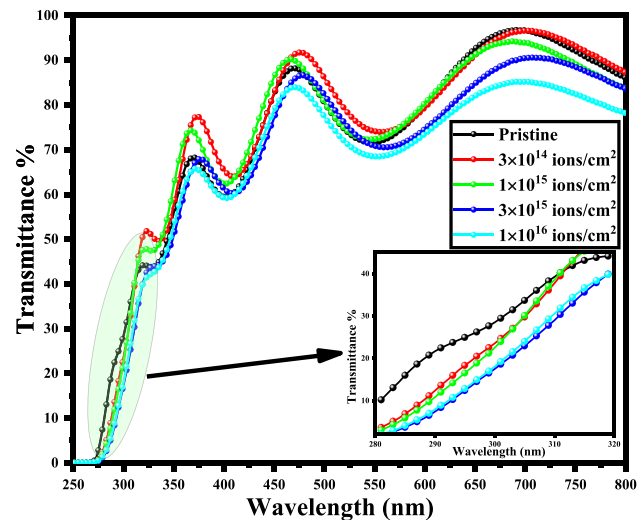


Fig. 4 Transmittance spectra of pristine and implanted MTO samples. Inset displays the shift in absorption edge towards higher wavelength

fluence implanted sample. Moreover, at higher fluence, the reduction in transmittance percentage is ascribed to the generation of defect levels within the bandgap [38] and scattering at the rough surface [36]. In addition, the thickness of pristine MTO film is evaluated using transmittance spectra, which is around 530 nm. The detailed evaluation procedure, using Swanepoel envelope method to determine the thickness, is shown elsewhere [39].

The transition of electrons in a crystal initiates at the absorption edge in the transmittance spectra, which indicates the minimum energy difference (energy bandgap, E_g) between conduction band minima and valence band maxima [40]. There is a sharp absorption edge observed below ~ 320 nm for the films due to the fundamental absorption in this region.

Moreover, a shift in the absorption edge towards the higher wavelength regime (shown in the inset of Fig. 4) with increasing the implantation fluence, indicating a decrease in the bandgap. Wood and Tauc's method [40] was employed to evaluate the bandgap of the films. The detailed procedure to estimate the bandgap is given in our earlier report [41]. Tauc's plot utilized to obtain the bandgap is depicted in Fig. 5a–e, and the variation is plotted in Fig. 5f. The bandgap of the pristine film is nearly 4.22 eV. Co ions implantation at 3×10^{14} ions/cm² fluence, leads to the narrowing of optical bandgap to 4.01 eV. A minor rise in optical bandgap to 4.03 eV is observed with the rise of fluence to 1×10^{15} ions/cm². Afterward, the bandgap again goes down to 3.96 eV upon increasing the fluence up to 3×10^{15} ions/cm². An upsurge in the implantation fluence to 1×10^{16} ions/cm² results in further shrinkage of the bandgap to 3.88 eV. Co ions implantation into the MTO matrix induces damage to the lattice, which creates defect levels leading to the reduction in bandgap [42]. Such a reduction in bandgap is also observed in SrVO₃ after implantation with Cu ions [43]. Furthermore, with an increase in fluence, more number of

defects created, since the lattice damage is proportional to the implantation fluence [44]. The implantation induced structural disorder in the films can also be revealed using Urbach tail. The exponential region in the absorption edge, referred to Urbach energy (E_u) reflects the tail of the band states (arised due to disorder), which are extended into the forbidden region [40], thereby decreasing the band-gap energy. The slope of the plot of $\ln\alpha$ vs energy (Fig. 6) was utilized to obtain the E_u , which is illustrated in inset of Fig. 6. Implantation at a fluence of 3×10^{14} ions/cm² leads to an increase in E_u from 0.21 (for pristine film) to 0.28 eV. Subsequently, the E_u is increased from 0.28 to 0.34 eV after an upsurge of implantation fluence from 1×10^{15} to 1×10^{16} ions/cm². The consistent growth in E_u with fluence can be attributed to the generation of additional tail states as a result of implantation stimulated distortion into the MTO lattice [42].

3.4 XPS analysis

XPS profile, as shown in Fig. 7, illustrates the chemical states of Mg, Ti, and O in the pristine and Co implanted MTO thin films. The survey scan was recorded in the binding energy (BE) range of 0–1350 eV. The BE scale was corrected using standard calibration by fixing the C 1s peak, which is located at a BE of 284.8 eV due to the presence of adventitious carbon from the atmosphere during experiment [45].

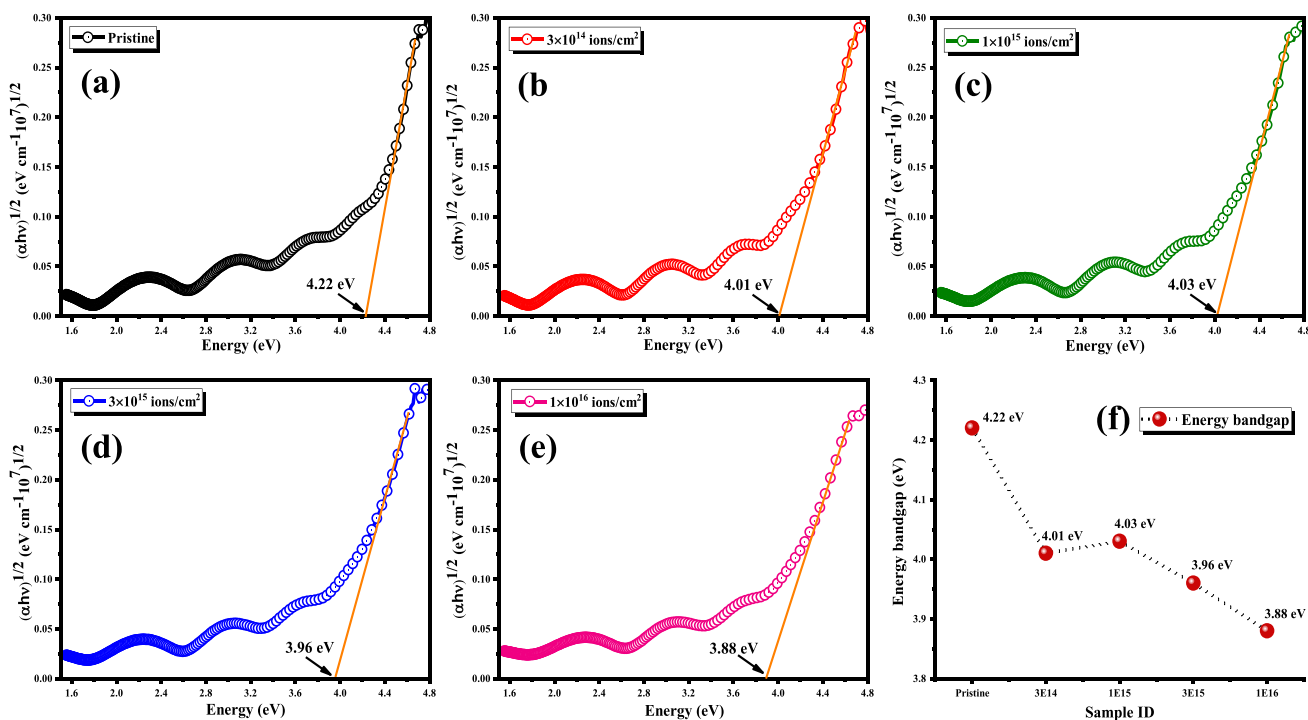


Fig. 5 a–e Tauc's plot, and f bandgap variation of pristine and implanted MTO thin films

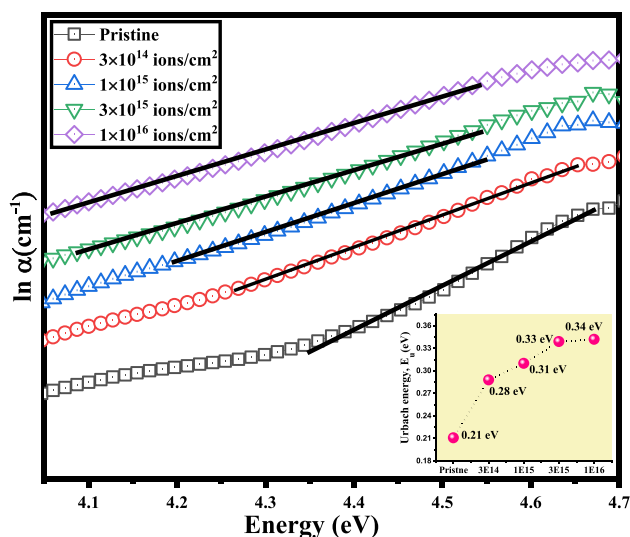


Fig. 6 Plot of $\ln \alpha$ vs energy for pristine and Co implanted samples. Inset shows the variation of Urbach energy (E_u) with fluence

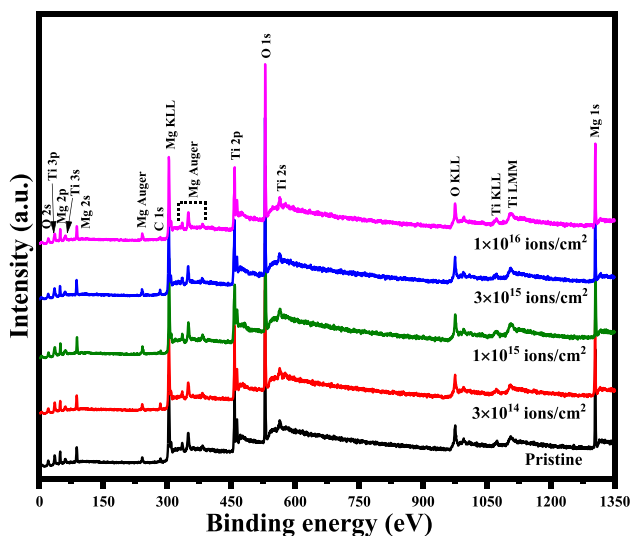


Fig. 7 XPS spectra of pristine and implanted MTO samples with Co ions at various fluences

The detailed spectra of Mg 2p, Ti 2p, and O 1s are taken in the BE range of 45 to 55 eV, 450 to 470 eV, and 526 to 535 eV, respectively, as shown in Fig. 8A–C. The fitting of the detailed XPS profile was done using CASA–XPS with Gaussian–Lorentzian product (GL) function. The XPS spectrum of Mg 2p corresponding to pristine and implanted MTO thin films is shown in Fig. 8A. The Mg 2p spectra show a peak lie at the binding energy of ~ 49.7 – 49.9 eV corresponds to the metallic magnesium [46].

The fitting of Ti 2p detailed spectra of pristine and Co implanted film at 3×10^{14} ions/cm², results in the two spin

orbit components, Ti 2p_{1/2} and Ti 2p_{3/2} [47]. Both the components were found to exist in +4 and +3 charge states, as shown in Fig. 8B.

The completely oxidized +4 states lie in the BE range ~ 464.4 – 464.5 eV and ~ 458.4 – 458.6 eV related to Ti 2p_{1/2} and Ti 2p_{3/2}, which is consistent with the earlier report [48]. While the +3 state corresponding to both the spin orbit components lie at the BE of ~ 462.6 – 462.9 eV and ~ 456.6 – 456.8 eV, respectively. The BE separation of the +4 state of Ti 2p_{1/2} and 2p_{3/2} is ~ 5.8 – 6.2 eV, which agrees with the results observed in the literature [49]. There is a slight decrease in the percentage of +4 states of spin orbit components of Ti 2p, while percentage of +3 states is observed to increase at a fluence of 3×10^{14} ions/cm². Moreover, upon enhancing the implantation fluence to 1×10^{15} ions/cm², a substantial enhancement of +3 state corresponds to both the spin orbit components is observed. In addition, +2 states are also observed to evolve at higher implantation fluence, which lie at the BE of 455.1–455.2 eV (for Ti 2p_{3/2}) and 461–461.3 eV (Ti 2p_{1/2}), respectively. A similar observation was also reported for the Ti 2p state of TiO₂ after ion implantation [33, 50]. The structural modification due to thermally induced lattice vibrations at higher implantation fluence associated with the increase in concentration of Ti³⁺ [51]. Moreover, an increase in the concentration of +3 as well as +2 states also corroborates the presence of oxygen deficient atmosphere [33, 52, 53]. In addition, implantation induces point defects which subsequently merges to generate defect complexes at higher implantation fluence [54] appeared as an enhancement of percentage composition corresponds to +3 state. A further rise in implantation fluence to 3×10^{15} and 1×10^{16} ions/cm², a slight reduction in the percentage composition of +3 and +2 states as compared to 1×10^{15} ions/cm² is observed. Such a large implantation fluence may leads to local temperature rise in the lattice resulting in migration of vacancies which recombine with defects present at the interstitial sites leading to the recovery of few lattice defects at the surface [55].

The detailed XPS spectra of O 1s corresponding to pristine and implanted MTO samples is shown in Fig. 8C.

O 1s (A) at the binding energy of ~ 530 – 530.1 eV with oxidation state -2, attributed to the lattice oxygen, while the peak situated at higher BE (~ 531.7 – 531.8 eV) is accredited to oxygen vacancies [46, 56, 57]. A slight increase in oxygen vacancies at a fluence of 1×10^{15} ions/cm², can be correlated with increase and generation of Ti³⁺ and Ti²⁺ states. On further implantation at higher fluences, i.e., 3×10^{15} and 1×10^{16} ions/cm², there is no significant variation in the oxygen vacancies.

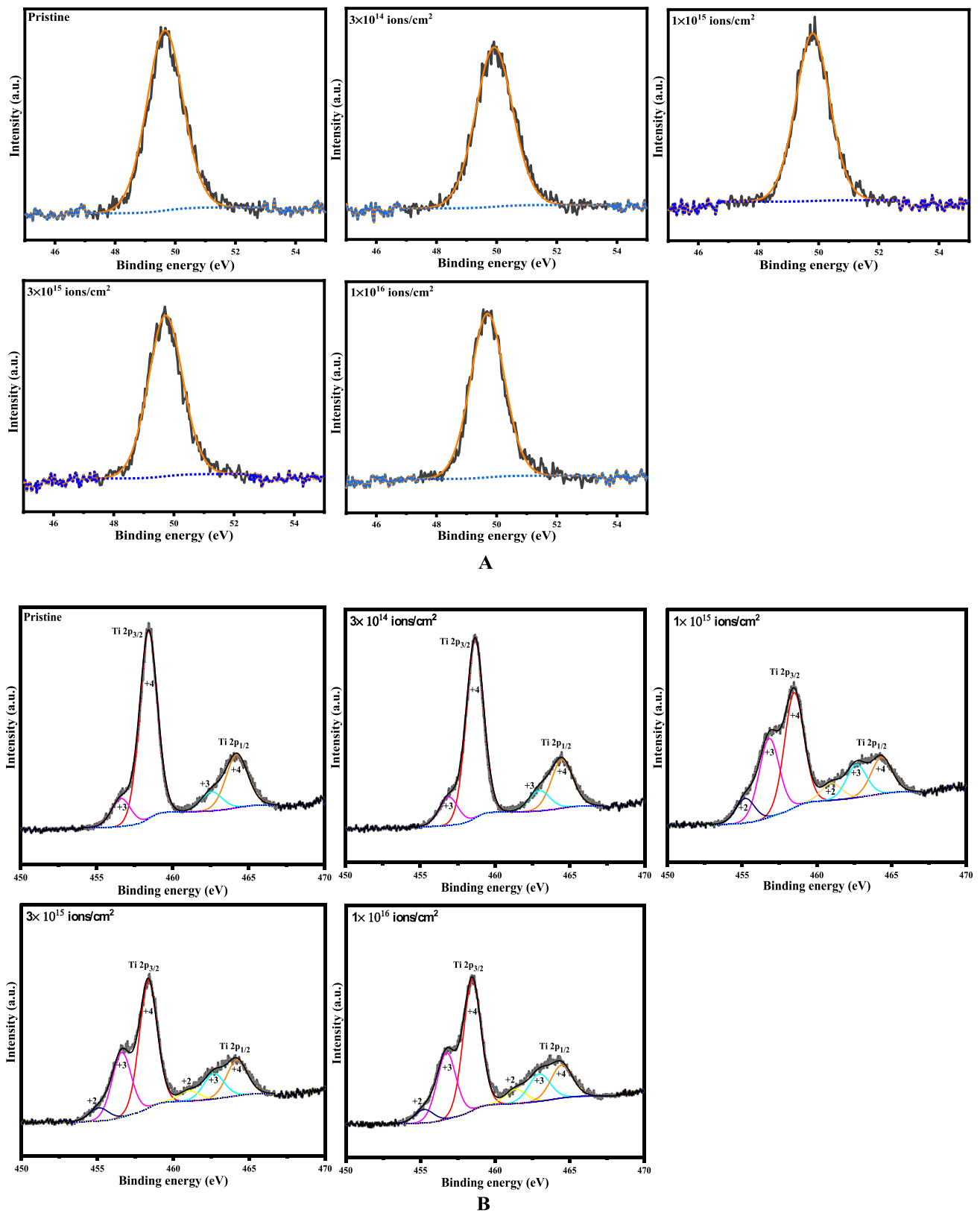


Fig. 8 **A** XPS spectra of Mg 2p for pristine and Co implanted MTO thin films. **B** XPS spectra of Ti 2p for pristine and Co implanted MTO thin films. **C** XPS spectra of O 1s for pristine and Co implanted MTO thin films

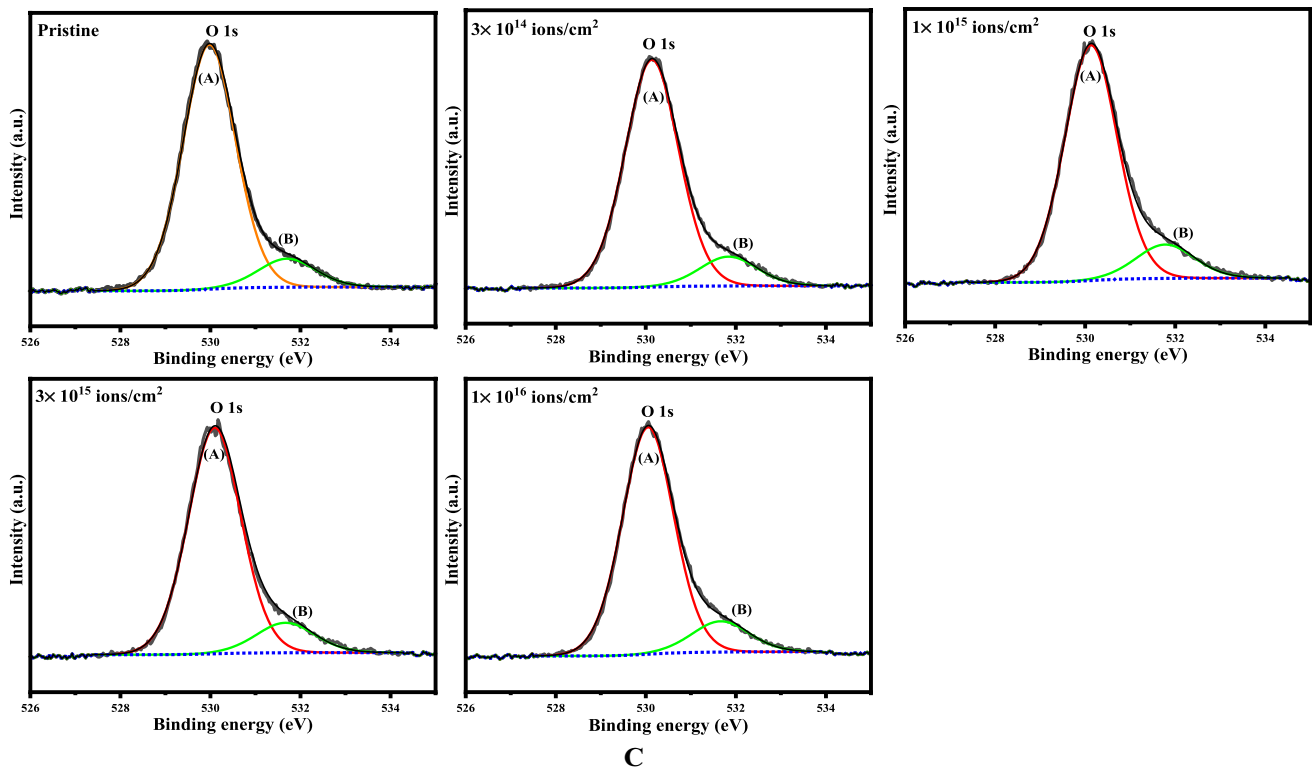


Fig. 8 (continued)

3.5 PL and TRPL study

Figure 9a demonstrates the PL emission spectra of pristine and implanted MTO thin films with Co ions. The spectra were taken in 340–680 nm wavelength range. The pristine MTO film shows a broad PL emission band extended in the range of 350–600 nm. The deconvoluted spectrum (Fig. 9b) indicates the possible emission centers in pristine MTO film. Different PL emission centers arise in MTO are probably due to the defects in the sample, since the emission centers lie well below the bandgap of MTO thin film. The structural complexity (order–disorder at long and short range) in pristine films is evident from the presence of PL emission. Essentially, MTO shows PL emission due to the order–disorder in the structure within the lattice network. The presence of intrinsic and extrinsic defects give rise to the disordered lattice, which creates additional energy states in-between the valence band and conduction band. During excitation, the generated defect levels facilitate the charge carriers trapping, which leads to the distinct PL emission in MTO [58].

The extrinsic defects present in MTO are related to the dislocation of Ti and Mg present in lattice former and modifier, results in the creation of complex clusters which act as trapping centers for charge carriers. The complex cluster formation in lattice former and lattice modifier network as well as the intrinsic disorder are demonstrated by E. A. V.

Ferri et al. [58]. The different types of structural defects in the disordered MTO system contribute to specific states within the forbidden gap, resulting in the generation of various luminescent centers [59]. Pristine MTO film shows near UV and visible emission, centered at 3.38 eV (~367 nm), 3.25 eV (~382 nm), 3.04 eV (~408 nm), 2.82 eV (~440 nm), 2.64 eV (~470 nm), 2.51 eV (~494 nm), and 2.32 eV (~534 nm). Each color represents a specific electronic transition, which is related to a particular structural arrangement. E. A. V. Ferri et al. showed that the $[\text{TiO}_5, V_O^x]$ complex cluster related to the deeper defects [58]. In addition, V. M. Longo et al. elucidated that $[\text{TiO}_5, V_O^\bullet]$ and $[\text{TiO}_5, V_O]$ complex clusters correspond to deep and shallow defects within the bandgap for SrTiO_3 [59]. The more energetic PL emission is probably related to shallow defects, while the deep defects lead to the low energy visible emission [59]. In addition, visible emission in MTO is preferentially due to the deep level defects, which are probably related to the lattice former [58]. Moreover, in other matrix, such as ZnO , the low energy visible emission is also resulted due to the deep level defects as depicted by R. G. Singh et al. and H. Gupta et al. [60, 61]. After implantation with Co ions at a fluence of 3×10^{14} ions/cm², PL intensity is observed to reduce significantly. During implantation, nuclear energy loss inside the MTO matrix facilitates the cascade collision, which results in the generation of large defect density.

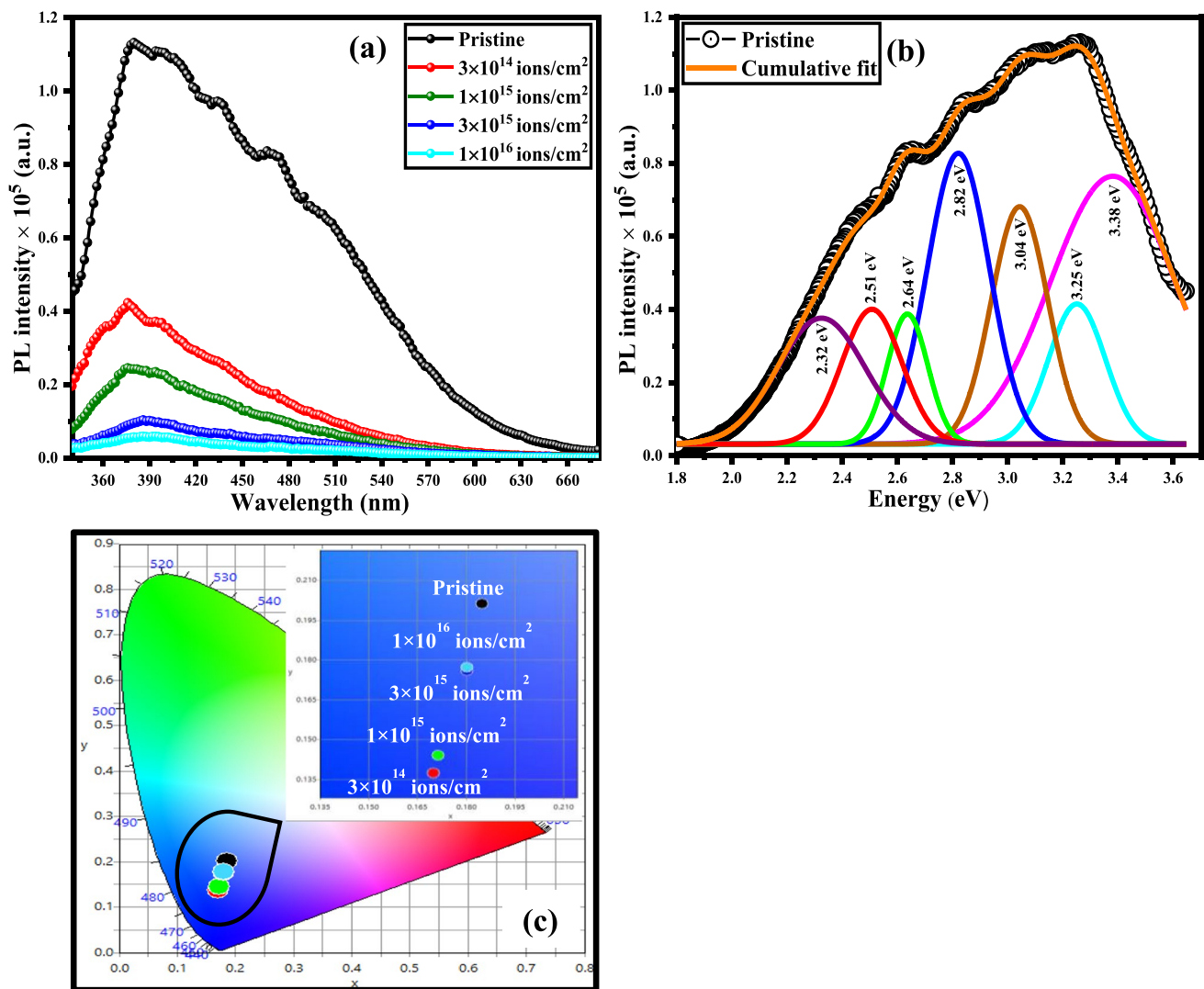


Fig. 9 **a** PL spectra of pristine and implanted MTO thin films **b** Deconvoluted PL spectrum of pristine sample **c** CIE chromaticity plot of pristine and implanted MTO samples

Typically the radiation damage due to implantation causes non-radiative defect centers. These non-radiative defects created inside the matrix may probably result in an effective decrease in PL intensity [62]. The dissipation of emission intensity can also be understood on the basis of increasing energy transfer between the dopants and defects due to increasing interaction between them. At higher fluence, a larger concentration of dopants results in a decrease in distance between defects and dopants, which further increases the interaction between them, resulting in overall dissipation of luminescence intensity [63]. Furthermore, an enhancement of fluence up to 1×10^{15} ions/cm², again quenches the peak intensity. There is no significant alteration in the peak position for samples implanted at fluence of 1×10^{15} and 3×10^{15} ions/cm². At higher fluence of 1×10^{16} ions/cm², a drastic reduction in PL emission intensity is observed due

to the generation of large number of non-radiative defect centers. The Commission International del' Eclairage (CIE) chromaticity plot indicating the color center, and color purity of the pristine and implanted samples displayed in Fig. 9c. The color coordinates for pristine film are (0.185, 0.201) and implanted films at different fluences of 3×10^{14} , 1×10^{15} , 3×10^{15} , and 1×10^{16} ions/cm² are (0.170, 0.137), (0.171, 0.144), (0.180, 0.176) and (0.180, 0.177), respectively. The observed chromaticity coordinates confirms the blue emission of MTO thin films with an insignificant shift in coordinates after increasing the implantation fluence.

The time-resolved PL spectra of pristine, and Co ions implanted MTO samples are illustrated in Fig. 10a. The decay profile was analyzed and fitted (Fig. 10b–f) using a double exponential function, which is displayed as [64]

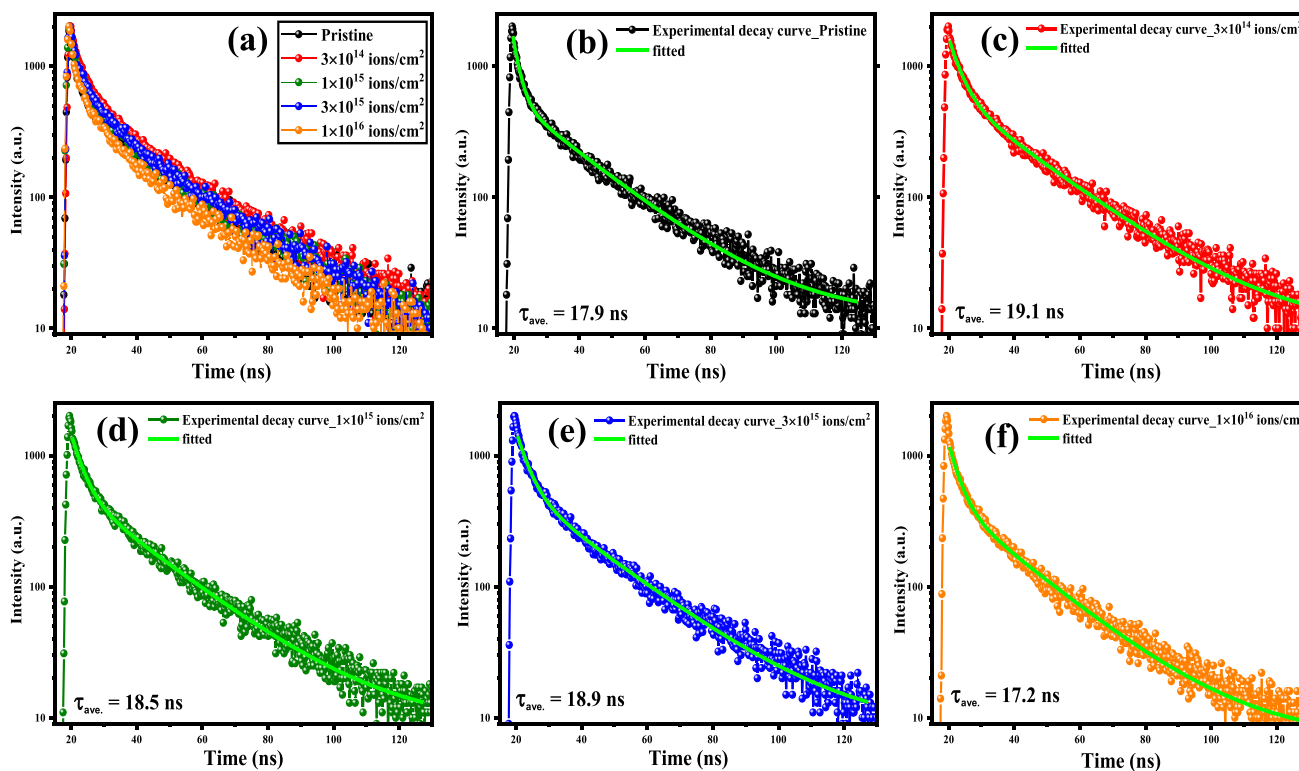


Fig. 10 a TRPL spectra, and b–f fitted TRPL plots for pristine and implanted MTO films

$$I(t) = A + B_1 e^{-t/\tau_1} + B_2 e^{-t/\tau_2} \quad (2)$$

where $I(t)$ is the intensity of luminescence at time t , τ_1 and τ_2 signify the lifetimes corresponding to fast and slow decay routes. The average decay lifetime (τ_{ave}) of pristine and implanted samples was estimated using τ_1 and τ_2 . The detailed procedure to calculate the τ_{ave} is discussed in our earlier report [41].

The implantation with Co ions at a fluence of 3×10^{14} ions/cm² leads to an increase in τ_{ave} from 17.9 ns (for pristine sample) to 19.1 ns. The prolonged lifetime of charge carriers depends on several factors, such as band structure, structural defects in the lattice, carriers' mobility, etc. The enhancement in lifetime is a result of suppression in recombination of charge carriers. The defect levels present at surface and bulk, acts as active trap centers for capturing the charge carriers. Instead of directly recombining with the holes in valence band, the carriers first trapped to defect levels below the conduction band. The trapping below the conduction band will be a non-radiative transition. Thereafter, the electrons undergo hopping from one defect to another until they find an emission center. Therefore, the presence of different defect levels facilitates the trapping of carriers for a considerable amount of time, resulting in the increase of lifetime of recombination of the charge carriers [63]. Furthermore,

increase in non-radiative recombinations, more likely at the surface, with increasing the fluence up to 1×10^{16} ions/cm² results in a reduction of average decay lifetime, which is consistent with the decrease in the PL intensity [65].

4 Conclusions

Co ions implantation engineered MTO thin films were studied to investigate the structural, surface, optical, chemical, and luminescent properties. Implantation leads to amorphization and generation of strain in the films. Moreover, a non-monotonous variation in the surface roughness is a result of adatoms' mobility over the surface, which varies with implantation fluence. A reduction in the grain size is resulted due to grain fragmentation upon implantation up to the fluence of 3×10^{15} ions/cm². Furthermore, an increment of grain size at higher fluence is a consequence of the agglomeration of smaller grains as a result of increased surface energy. The optical transmittance of the film implanted at a fluence of 3×10^{14} ions/cm² is slightly higher than the pristine sample due to its comparatively smoother surface (less roughness). While, a reduction in transmittance with further rise in fluence from 1×10^{15} to 1×10^{16} ions/cm² is observed. Structural modification at higher implantation fluence leads to the increase in composition of +3 states and generation

of +2 states corresponds to spin orbit components of Ti 2p. The luminescent properties are found to be strongly dependent upon types of complex clusters, which are related to deep and shallow defects. The pristine film possesses luminescent band extended from near UV to visible region. Implantation quenches the PL emission intensity due to the generation of non-radiative defect centres. The presence of different trap states probably leads to the enhancement in the average decay lifetime of implanted samples. Therefore, different complex clusters, vacancies, and the defects related to Ti and O in MTO are found to be sensitive to the implantation fluence, which further affects the optical and luminescent properties of MTO thin films.

Acknowledgements DN acknowledges Council of Scientific and Industrial Research, New Delhi, India for providing CSIR–SRF fellowship. NSR thanks Inter-University Accelerator Centre (IUAC), New Delhi, India for the ion implantation facility under project number UFR—64332. We are also thankful to Materials Research Centre, MNIT Jaipur for synthesis and characterization facilities. Authors are grateful to Prof. Kanupriya Sachdev and Dr. Kamalendra Awasthi, Department of Physics, MNIT Jaipur, Rajasthan, for annealing and UV–Vis–NIR spectroscopy facilities.

Data availability All data generated or analysed during this study are included in this published article.

Declarations

Conflict of interest The authors declare that they have no conflict of interest.

References

- E. Korkmaz, N.O. Kalaycioglu, V.E. Kafadar, Yellow phosphors doping with Gd^{3+} , Tb^{3+} and Lu^{3+} in $MTiO_3$ ($M = Mg$ and Sr) luminescence properties. *Bull. Mater. Sci.* **36**, 1079 (2013)
- X.C. Liu, R. Hong, C. Tian, Tolerance factor and the stability discussion of ABO_3 -type ilmenite. *J Mater Sci: Mater Electron* **20**, 323 (2009)
- X. Zhou, Y. Yuan, L. Xiang, Y. Huang, Synthesis of $MgTiO_3$ by solid state reaction and characteristics with addition. *J. Mater. Sci.* **42**, 6628 (2007)
- K. Wakino, Recent development of dielectric resonator materials and filters in japan. *Ferroelectrics* **91**, 69 (1989)
- J. Zhang, Z. Yue, Y. Luo, L. Li, $MgTiO_3/TiO_2/MgTiO_3$: An ultrahigh-Q and temperature-stable microwave dielectric ceramic through cofired trilayer architecture. *Ceram. Int.* **44**, 21000 (2018)
- C.L. Huang, C.L. Pan, Structure and electrical properties of $MgTiO_3$ thin films deposited by RF magnetron sputtering. *J. Vac. Sci. Technol. A* **22**, 2440 (2004)
- C. S. Hwang, K. Do, C. H. Lee, Taegu, Ferroelectric structure including $MgTiO_3$ passivation. United States Patent 5834804 (1998)
- L. Wang, G. Yang, S. Peng, J. Wang, D. Ji, W. Yan, S. Ramakrishna, Fabrication of $MgTiO_3$ nanofibers by electrospinning and their photocatalytic water splitting activity. *Int. J. Hydrogen Energy* **42**, 25882 (2017)
- R.S. Yadav, Monika, E. Rai, L.P. Purohit, S.B. Rai, Realizing enhanced downconversion photoluminescence and high color purity in Dy doped $MgTiO_3$ phosphor in presence of Li^+ ion. *J. Lumin.* **217**, 116810 (2020)
- J. Zhang, J. Yin, P. Liu, B. Gao, L. Bie, Preparation and luminescent properties of $MgTiO_3:Eu^{3+}$ phosphor for white LEDs. *J. Rare Earths* **30**, 1009 (2012)
- N. Kuganathan, P. Iyngaran, R. Vovk, A. Chronos, Defects, dopants and Mg diffusion in $MgTiO_3$. *Sci. Rep.* **9**, 4394 (2019)
- J.H. Sohn, Y. Inaguma, S.O. Yoon, M. Itoh, T. Nakamura, S.J. Yoon, H.J. Kim, Microwave dielectric characteristics of ilmenite-type titanates with high Q values. *Jpn. J. Appl. Phys.* **33**, 5466 (1994)
- T.S. Kumar, P. Gogoi, S. Bhasaiah, K.C.J. Raju, D. Pamu, Structural, optical and microwave dielectric studies of Co doped $MgTiO_3$ thin films fabricated by RF magnetron sputtering. *Mater. Res. Express* **2**, 056403 (2015)
- T.S. Kumar, P. Gogoi, S. Thota, D. Pamu, Structural and dielectric studies of Co doped $MgTiO_3$ thin films fabricated by RF magnetron sputtering. *AIP Adv.* **4**, 067142 (2014)
- Y.N. Shieh, Y.Y. Chang, Influence of cobalt ion implantation on optical properties of titanium dioxide thin films. *Thin Solid Films* **518**, 7464 (2010)
- M. I. Khan, M. Sabir, G. M. Mustafa, M. Fatima, A. Mahmood, S. A. Abubshaitd, H. A. Abubshait, M. Iqbal 300 keV cobalt ions irradiations effect on the structural, morphological, optical and photovoltaic properties of Zn doped TiO_2 thin films based dye sensitized solar cells. *Ceram. Int.* **46**, 16813 (2020)
- J. Xu, S. Shi, L. Li, X. Zhang, Y. Wang, X. Chen, J. Wang, L. Lv, F. Zhang, W. Zhong, Structural, optical, and ferromagnetic properties of Co-doped TiO_2 films annealed in vacuum. *J. Appl. Phys.* **107**, 053910 (2010)
- R. Kumar, F. Singh, B. Angadi, J.W. Choi, W.K. Choi, K. Jeong, J.H. Song, M.W. Khan, J.P. Srivastava, A. Kumar, R.P. Tandon, Single phase formation of Co-implanted ZnO thin films by swift heavy ion irradiation: Optical studies. *J. Appl. Phys.* **100**, 113708 (2006)
- S. Zhou, K. Potzger, G. Talut, H. Reuther, J.V. Borany, R. Grotzschel, W. Skorupa, M. Helm, J. Fassbender, Fe-implanted ZnO: Magnetic precipitates versus dilution. *J. Appl. Phys.* **103**, 023902 (2008)
- I.P. Jain, G. Agarwal, Ion beam induced surface and interface engineering. *Surf. Sci. Rep.* **66**, 77 (2011)
- Kriti, P. Kaur, S. Chalotra, R. Nongjai, I. Sulania, A. Kandasami, D. P. Singh, Effect of 150 keV Ti^{+} ion implantation on the structural, optical, and electrical properties of nonstoichiometric $WO_{2.72}$ thin film. *Mater. Res. Bull.* **145**, 111566 (2022)
- D.R. Kumar, K.S. Ranjith, Y. Haldorai, A. Kandasami, R.T.R. Kumar, Nitrogen-implanted ZnO Nanorod arrays for visible light photocatalytic degradation of a pharmaceutical drug acetaminophen. *ACS Omega* **4**, 11973 (2019)
- A. Audren, A. Hallen, M.K. Linnarsson, G. Possnert, Damage recovery in ZnO by post-implantation annealing. *Nucl. Inst. Methods Phys. Res. B* **268**, 1842 (2010)
- R. Shyam, D. Negi, K. Shekhawat, F. Singh, D. Devi, P. Vashishtha, G. Gupta, S. Pandey, P. Dobbidi, S.R. Nelamarri, Tailoring of physical properties of (K, Na)NbO₃ thin films using lithium ion implantation. *Results Phys.* **47**, 106330 (2023)
- A.M. Galvan, C.T. Cruz, Effect of metal-ion doping on the optical properties of nanocrystalline ZnO thin films. *J. Appl. Phys.* **99**, 014306 (2006)
- C. Liu, B. Mensching, K. Volz, B. Rauschenbach, Lattice expansion of Ca and Ar ion implanted GaN. *Appl. Phys. Lett.* **71**, 2313 (1997)
- P. Mallick, C. Rath, J. Prakash, D.K. Mishra, R.J. Choudhary, D.M. Phase, A. Tripathi, D.K. Avasthi, D. Kanjilal, N.C. Mishra, Swift heavy ion irradiation induced modification of

- the microstructure of NiO thin films. *Nucl. Inst. Methods Phys. Res. B* **268**, 1613 (2010)
28. S. Shanmugan, D. Mutharasu, An effect of N^+ ion bombardment on the properties of CdTe thin films. *Radiat. Phys. Chem.* **81**, 201 (2012)
 29. B.D. Cullity, *Elements of X-Ray Diffraction*, 2nd Edition, Addison-Wesley, 1978
 30. C. Suryanarayana, M.G. Norton, *X-Rays and Diffraction* (Springer, US, Boston, 1998)
 31. U. Valbusa, C. Boragno, F.B.D. Mongeot, Nanostructuring surfaces by ion sputtering. *J. Phys. Condens. Matter* **14**, 8153 (2002)
 32. A. Galdikas, Non-monotonous dependence of surface roughness on factors influencing energy of adatoms during thin island film growth. *Surf. Sci.* **600**, 2705 (2006)
 33. V. Solanki, S. Majumder, I. Mishra, P. Dash, C. Singh, D. Kanjilal, S. Varma, Enhanced anomalous photo-absorption from TiO_2 nanostructures. *J. Appl. Phys.* **115**, 124306 (2014)
 34. S.R. Joshi, A. Chanda, D. Kanjilal, S. Varma, Scaling studies of self-affine nanopatterned TiO_2 surfaces created via ion implantation. *Thin Solid Films* **639**, 145 (2017)
 35. D.C. Agarwal, R.S. Chauhan, D.K. Avasthi, S.A. Khan, D. Kabiraj, I. Sulania, Formation of self-affine nanostructures on ZnO surfaces by swift heavy ions. *J. Appl. Phys.* **104**, 024304 (2008)
 36. D. Song, E.C. Cho, G. Conibeer, Y.H. Cho, Y. Huang, S. Huang, C. Flynn, M.A. Green, Fabrication and characterization of Si nanocrystals in SiC matrix produced by magnetron cosputtering. *J. Vac. Sci. Technol. B* **25**, 1327 (2007)
 37. T.G. Lei, H.H. Bo, S.J. Da, Effects of microstructure of TiO_2 thin films on optical band gap energy. *Chin. Phys. Lett.* **22**, 1787 (2005)
 38. G.D. Cody, T. Tiedje, B. Abeles, B. Brooks, Y. Goldstein, Disorder and the optical-absorption edge of hydrogenated amorphous silicon. *Phys. Rev. Lett.* **47**, 1480 (1981)
 39. M.M. Soraya, Structural and optical properties of $Se_{85-x}Te_{15}In_x$ chalcogenide thin films for optoelectronics. *Appl. Phys. A* **126**, 590 (2020)
 40. J. Tauc, *Optical properties of amorphous Semiconductors, Amorphous and liquid semiconductors* (Springer, Boston, MA, 1974)
 41. D. Negi, R. Shyam, P. Vashishtha, G. Gupta, F. Singh, S.R. Nelamarri, Impact of high energy ion irradiation on structural, morphological, optical and photoluminescence properties of $MgTiO_3$ thin films. *J. Lumin.* **249**, 119051 (2022)
 42. A. Majid, A. Ali, Band tailing effects in neon-implanted GaN. *J. Appl. Phys.* **106**, 123528 (2009)
 43. H. Saraswat, S. Chaudhary, M. Varshney, D. Devi, F. Singh, S.O. Won, H.J. Shin, A. Sharma, 150 KeV Cu- ion- implantation in $SrVO_3$ thin films: A study of Cu induced defect states. *Vacuum* **181**, 109655 (2020)
 44. A. Shah, A. Mahmood, Effect of Cr implantation on structural and optical properties of AlN thin films. *Physica B* **407**, 3987 (2012)
 45. G. Greczynski, L. Hultman, C 1s peak of adventitious carbon aligns to the vacuum level: Dire consequences for material's bonding assignment by photoelectron spectroscopy. *ChemPhysChem* **18**, 1507 (2017)
 46. H.B. Yao, Y. Li, A.T.S. Wee, An XPS investigation of the oxidation/corrosion of melt spun Mg. *Appl. Surf. Sci.* **158**, 112 (2000)
 47. K. Ami, T. Isobe, M. Senna, Physical and chemical interactions in multi-component composite particles prepared by mechanical stressing. *Powder Technol.* **100**, 46 (1998)
 48. D. Pukazhselvan, N. Nasani, T. Yang, D. Ramasamy, A. Shaula, D.P. Fagg, Chemically transformed additive phases in Mg_2TiO_4 and $MgTiO_3$ loaded hydrogen storage system MgH_2 . *Appl. Surface Sci.* **472**, 99 (2019)
 49. D. Jaeger, J. Patscheider, A complete and self-consistent evaluation of XPS spectra of TiN. *J. Electron Spectros. Relat. Phenomena* **185**, 523 (2012)
 50. A. Manna, A. Barman, S.R. Joshi, B. Satpati, P. Dash, A. Chattaraj, S.K. Srivastava, P.K. Sahoo, A. Kanjilal, D. Kanjilal, S. Varma, The effect of Ti^+ ion implantation on the anatase-rutile phase transformation and resistive switching properties of TiO_2 thin films. *J. Appl. Phys.* **124**, 155303 (2018)
 51. F. Guillemot, M.C. Port, C. Labrugere, Ch. Baquey, Ti^{4+} to Ti^{3+} Conversion of TiO_2 Uppermost Layer by Low-Temperature Vacuum Annealing: Interest for Titanium Biomedical Applications. *J. Colloid Interface Sci.* **255**, 75 (2002)
 52. Z. Fang, H. Yang, H. Yang, Z. Xiong, X. Zhang, P. Zhao, B. Tang, Ilmenite-type $MgTiO_3$ ceramics by complex $(Mn_{1/2}W_{1/2})^{4+}$ cation co-substitution producing improved microwave characteristics. *Ceram. Int.* **47**, 21388 (2021)
 53. I. Spasojevic, G. Sauthier, J.M. Caicedo, A. Verdager, N. Domingo, Oxidation processes at the surface of $BaTiO_3$ thin films under environmental conditions. *Appl. Surf. Sci.* **565**, 50288 (2021)
 54. B.K. Ostafychuk, V.D. Fedoriv, I.P. Yaremiy, O.Z. Garpul, V.V. Kurovets, I.C. Yaremiy, Implantation of single crystalline iron garnet thin films with He^+ , B^+ , and Si^+ ions. *Phys. Status Solidi A* **208**, 2108 (2011)
 55. X. Wang, J. Li, J. Wang, J. Song, F. Zhao, H. Tang, B.S. Li, A.L. Xiong, Microstructure investigation of damage recovery in SiC by swift heavy ion irradiation. *Mater. Design Process. Commun.* **1**, e87 (2019)
 56. M.J. Jackman, A.G. Thomas, C. Muryn, Photoelectron spectroscopy study of stoichiometric and reduced anatase $TiO_2(101)$ surfaces: The effect of subsurface defects on water adsorption at near-ambient pressures. *J. Phys. Chem.* **119**, 13682 (2015)
 57. J.C. Dupin, D. Gonbeau, P. Vinatier, A. Levasseur, Systematic XPS studies of metal oxides, hydroxides and peroxides. *Phys. Chem. Chem. Phys.* **2**, 1319 (2000)
 58. E.A.V. Ferri, T.M. Mazzo, V.M. Longo, E. Moraes, P.S. Pizani, M.S. Li, J.W.M. Espinosa, J.A. Varela, E. Longo, Very intense distinct blue and red photoluminescence emission in $MgTiO_3$ thin films prepared by the polymeric precursor method: An experimental and theoretical approach. *J. Phys. Chem. C* **116**, 15557 (2012)
 59. V.M. Longo, A.T.D. Figueiredo, S.D. Lazaro, M.F. Gurgel, M.G.S. Costa, C.O.P. Santos, J.A. Varela, E. Longo, V.R. Mastelaro, F.S.D. Vicente, A.C. Hernandez, R.W.A. Franco, Structural conditions that leads to photoluminescence emission in $SrTiO_3$: An experimental and theoretical approach. *J. Appl. Phys.* **104**, 023515 (2008)
 60. R.G. Singh, H. Gupta, R.M. Mehra, F. Singh, Tuning of defects induced visible photoluminescence by swift heavy ion irradiation and thermal annealing in zinc oxide films. *Radiat. Phys. Chem.* **183**, 109400 (2021)
 61. H. Gupta, J. Singh, R.N. Dutt, S. Ojha, S. Kar, R. Kumar, V.R. Reddy, F. Singh, Defects induced photoluminescence from gallium doped zinc oxide thin films: Influence of doping and energetic ion irradiation. *Phys. Chem. Chem. Phys.* **21**, 15019 (2019)
 62. I. Sakaguchi, D. Park, Y. Takata, S. Hishita, N. Ohashi, H. Haneda, T. Mitsuhashi, An effect of annealing on In implanted ZnO. *Nucl. Inst. Methods Phys. Res. B* **206**, 153 (2003)
 63. B. Choudhury, A. Choudhury, Luminescence characteristics of cobalt doped TiO_2 nanoparticles. *J. Lumin.* **132**, 178 (2012)
 64. M.R. Wagner, G. Callsen, J.S. Reparaz, J.H. Schulze, R. Kirste, M. Cobet, I.A. Ostapenko, S. Rodt, C. Nenstiel, M. Kaiser, A. Hoffmann, Bound excitons in ZnO: Structural defect complexes

- versus shallow impurity centers. *Phys. Rev. B* **84**, 035313 (2011)
65. J. Panigrahi, P.K. Singh, G. Gupta, Vandana, Growth and luminescence characteristics of zinc oxide thin films deposited by ALD technique. *J. Lumin.* **233**, 117797 (2021)

Springer Nature or its licensor (e.g. a society or other partner) holds exclusive rights to this article under a publishing agreement with the author(s) or other rightsholder(s); author self-archiving of the accepted manuscript version of this article is solely governed by the terms of such publishing agreement and applicable law.

Publisher's Note Springer Nature remains neutral with regard to jurisdictional claims in published maps and institutional affiliations.